ADMET & DMPK **14** (2026) 3535*; doi: https://doi.org/10.5599/admet.3535*

ADMET
Open Access : ISSN : 1848-7718
http://www.pub.iapchem.org/ojs/index.php/admet

Original scientific paper

Simultaneous electrochemical determination of acetaminophen and ciprofloxacin in pharmaceutical formulations using a holmium-modified UiO-66 metal-organic framework electrode

Nguyen Quang Man[1], Pham Thi Huyen Thoa[2,3], Phan Tu Quy[3], Tran Thi Phuong Nga[2], Cao Van Hoang[4], Le Van Thanh Son[5], Le Thi Hong Phong[6], Pham Khac Lieu[2], Le Lam Son[2,*] and Dinh Quang Khieu[2,*]

[1]*University of Medicine and Pharmacy, Hue University, Hue City, Vietnam*
[2]*University of Sciences, Hue University, Hue City, Vietnam*
[3]*Department of Natural Sciences & Technology, Tay Nguyen University, Dak Lak Province, Vietnam*
[4]*Faculty of Natural Science, Quy Nhon University, Gialai Province, Vietnam*
[5]*University of Education and Science, The University of Danang, Danang city, Vietnam*
[6]*Institute of Materials Sciences, Vietnam Academy of Science and Technology, 18 Hoang Quoc Viet, Cau Giay, Hanoi City, Vietnam*

Corresponding Authors: E-mail: *lelamson@hueuni.edu.vn; *dqkhieu@hueuni.edu.vn

Received: June 1, 2026; Revised: August 9, 2026; Published: August 15, 2026

Abstract

Background and purpose: The simultaneous determination of acetaminophen (ACE) and ciprofloxacin (CIP) is of considerable importance for pharmaceutical quality control, necessitating the development of sensitive and reliable electrochemical sensors. In this study, a holmium-modified UiO-66 metal-organic framework (Ho/UiO-66) was synthesized and evaluated as an electrode modifier for the simultaneous electrochemical determination of ACE and CIP. **Experimental approach:** Ho/UiO-66 was synthesized via a solvothermal method and characterized by X-ray diffraction, Fourier-transform infrared spectroscopy, Raman spectroscopy, nitrogen adsorption-desorption analysis, scanning electron microscopy, transmission electron microscopy and energy-dispersive X-ray mapping. The electrochemical behaviour of ACE and CIP at the Ho/UiO-66-modified glassy carbon electrode (Ho/UiO-66/GCE) was investigated using cyclic voltammetry and differential pulse voltammetry. The effects of solution pH, scan rate, accumulation potential, and accumulation time were systematically optimized. **Key results:** The characterization results demonstrated the successful incorporation of Ho species while preserving the crystalline structure of UiO-66. Among the investigated materials, Ho/UiO-66 (3/100 molar ratio) exhibited the most favourable combination of crystallinity, porosity and electrochemical performance, and was therefore selected for sensor fabrication. Under the optimized conditions, well-resolved oxidation peaks for ACE and CIP were obtained, enabling their simultaneous determination without mutual interference. The oxidation processes were found to be predominantly diffusion-controlled. The developed sensor exhibited satisfactory analytical performance with wide linear concentration ranges, low detection limits, satisfactory repeatability, reproducibility, and long-term stability. The sensor was applied to the determination of ACE and CIP in real pharmaceutical samples with satisfactory recoveries. The analytical results showed good agreement with those obtained using the reference high-performance liquid chromatography method. **Conclusion:** The proposed Ho/UiO-66/GCE sensor provides a reliable and practical platform for the simultaneous electrochemical determination of ACE and CIP, demonstrating its potential applicability for pharmaceutical analysis.

Keywords

Differential pulse voltammetry; drug quality control; metal-organic frameworks; multiplex sensing; rare-earth doping; standard addition method

Introduction

Acetaminophen (ACE) is one of the most widely used analgesic and antipyretic drugs worldwide. Owing to its high efficacy and relatively low cost, ACE is extensively employed for the treatment of pain and fever [1]. However, excessive intake may cause severe hepatotoxicity and nephrotoxicity [2]. Ciprofloxacin (CIP) is a broad-spectrum fluoroquinolone antibiotic commonly prescribed for the treatment of various bacterial infections [3,4]. Although highly effective, the widespread use of CIP has raised concerns regarding the emergence of antimicrobial resistance and the occurrence of pharmaceutical residues in environmental systems. Therefore, reliable analytical methods for the determination of ACE and CIP are important for pharmaceutical quality control and regulatory monitoring. The simultaneous determination of multiple pharmaceutical compounds has attracted increasing attention because it can improve analytical throughput while reducing analysis time, reagent consumption, and operational costs. The ability to distinguish and quantify different electroactive compounds in a single measurement is considered an important criterion for evaluating the performance of advanced electrochemical sensing materials. In this context, ACE and CIP, representing two widely used classes of pharmaceuticals, can serve as suitable model analytes for investigating the multiplex detection capability of novel electrode materials.

Various analytical techniques have been reported for the determination of ACE, including high-performance liquid chromatography (HPLC) [5,6], reversed-phase high-performance liquid chromatography (RP-HPLC) [7,8], and liquid chromatography-tandem mass spectrometry (LC-MS/MS) [9]. These methods generally provide high sensitivity and selectivity; however, they often require expensive instrumentation, complicated sample preparation procedures, and relatively long analysis times.

Similarly, several analytical approaches have been developed for the determination of CIP, as HPLC [10,11], RP-HPLC [12,13], LC-MS/MS [14,15], and fluorescence spectroscopy [16,17]. Although these techniques offer reliable analytical performance, their practical application may be limited by high operational costs, labour-intensive sample pretreatment, and the need for skilled operators. In contrast, electrochemical methods have emerged as attractive alternatives because of their simplicity, rapid response, low cost, portability, and suitability for real-time monitoring. Nevertheless, the simultaneous electrochemical determination of ACE and CIP remains challenging due to the overlapping oxidation signals of the analytes and the limited sensitivity of conventional electrode materials.

To improve analytical performance, considerable efforts have been devoted to the design of advanced electrode modifiers with large active surface areas, abundant catalytic sites, and enhanced charge-transfer properties. Among the various functional materials investigated, metal-organic frameworks (MOFs) have attracted considerable attention for their exceptionally high porosity, tuneable pore structures, structural diversity, and chemical versatility. MOFs possess ordered crystalline architectures formed through the coordination of metal ions or clusters with organic ligands, enabling the rational design of materials with tailored physicochemical properties. These unique characteristics have led to their widespread applications in electrochemical sensing [18,19]. Among the numerous MOF families, UiO-66, a zirconium-based MOF composed of $Zr_6O_4(OH)_4$ clusters and terephthalic acid linkers, is particularly attractive for its remarkable thermal stability, chemical robustness, and high surface area. Moreover, the strong Zr-O bonds confer exceptional resistance to acidic and alkaline environments, making UiO-66 a suitable candidate for electrochemical applications [20]. However, pristine UiO-66 still suffers from relatively low intrinsic electrical conductivity and limited electrocatalytic activity, which may limit its analytical performance when used directly as an electrode modifier [21].

Recently, defect engineering and metal-ion incorporation have emerged as effective approaches for improving the electrochemical properties of MOFs [22]. The introduction of foreign metal ions can alter the electronic environment, generate additional active sites, increase structural defects, and facilitate charge transfer. In particular, rare-earth ions have attracted increasing attention because of their unique electronic configurations, variable coordination environments, strong Lewis acidity, and catalytic properties. Incorporating rare-earth elements into MOF structures may modify adsorption behaviour and electron-transfer processes, thereby enhancing sensing performance [23].

Among the lanthanide series, holmium ions (Ho^{3+}), characterized by their partially filled 4f orbitals and strong Lewis acidity, can modify the electronic environment of the framework [24], generate additional active sites, and facilitate electron-transfer processes, thereby enhancing the electrochemical performance of the resulting material [25,26]. In addition, Ho-containing materials have demonstrated attractive performance in photocatalysis, adsorption, luminescence, and electrochemical applications. Despite these advantages, studies concerning Ho-functionalized UiO-66 materials remain scarce, and their application in electrochemical sensing has not been extensively explored. Furthermore, to the best of our knowledge, the simultaneous electrochemical determination of ACE and CIP using Ho-modified UiO-66 has not yet been reported. Motivated by these considerations, a series of Ho-modified UiO-66 materials with varying Ho/Zr molar ratios were synthesized via solvothermal synthesis. The synthesized materials were subsequently employed as electrode modifiers for the simultaneous electrochemical determination of ACE and CIP. The effects of Ho incorporation on the physicochemical and electrochemical properties of UiO-66 were investigated, and the analytical performance of the resulting Ho/UiO-66-modified electrode was evaluated in terms of sensitivity, selectivity, precision, stability, and practical applicability.

Experimental

Chemicals and reagents

Zirconium(IV) chloride ($ZrCl_4$), terephthalic acid (H_2BDC), N,N-dimethylformamide (DMF), holmium(III) oxide (Ho_2O_3), acetaminophen (ACE), ciprofloxacin (CIP), potassium ferricyanide ($K_3[Fe(CN)_6]$), potassium ferrocyanide ($K_4[Fe(CN)_6]$), potassium chloride (KCl), phosphoric acid (H_3PO_4), boric acid (H_3BO_3), acetic acid (CH_3COOH), sodium hydroxide (NaOH), and ethanol were purchased from Sigma-Aldrich (Germany). All chemicals were of analytical grade and used as received without further purification.

Britton-Robinson buffer solution (BRS, 0.02 M) was prepared from phosphoric acid, boric acid and acetic acid, and the pH was adjusted using 0.1 M NaOH.

Synthesis of holmium-modified UiO-66 metal-organic framework

A series of Ho-modified UiO-66 materials were synthesized by a solvothermal method. Briefly, 0.0530 g of $ZrCl_4$ and 0.0380 g of terephthalic acid (H_2BDC) were dissolved in 5 mL of DMF under magnetic stirring to obtain a homogeneous solution [27]. A predetermined amount of $HoCl_3$ solution, prepared by dissolving Ho_2O_3 in HCl, was then added to the precursor mixture to obtain Ho/Zr molar ratios of 1/100, 3/100, 5/100, and 7/100.

The resulting mixture was transferred into a Teflon-lined stainless-steel autoclave and heated at 120 °C for 36 h. After cooling naturally to room temperature, the obtained solid was collected by centrifugation, washed several times with DMF and ethanol to remove unreacted precursors, and dried at 60 °C overnight. The synthesized materials were denoted as Ho/UiO-66 (1/100), Ho/UiO-66 (3/100), Ho/UiO-66 (5/100) and Ho/UiO-66 (7/100), respectively.

Material characterization

The crystal structures of the synthesized materials were examined by X-ray diffraction (XRD) using a Bruker D8 Advance diffractometer (Bruker, Germany). Fourier-transform infrared spectroscopy (FT-IR, Shimadzu Prestige-21, Japan) and Raman spectroscopy (XploRA™ PLUS, Horiba, Japan) were employed to investigate the chemical bonding and vibrational characteristics of the materials. The textural properties, including the specific surface area and pore structure, were determined from nitrogen adsorption-desorption isotherms using the Brunauer-Emmett-Teller (BET) method on a Tristar-3030 system (Micromeritics, USA).

The morphology and microstructure of the samples were characterized by field-emission scanning electron microscopy (FESEM, Hitachi S-4800, Japan) and transmission electron microscopy (TEM, JEM-1010, JEOL, Japan). The elemental composition and elemental distribution were analysed using an energy-dispersive X-ray spectroscopy (EDX) system coupled with elemental mapping attached to the FESEM instrument.

Preparation of modified electrodes

Prior to modification, the glassy carbon electrode (GCE, diameter 3 mm) was polished sequentially using alumina slurries, rinsed thoroughly with water, and sonicated in 1 M HNO_3 solution and absolute ethanol.

A suspension of Ho/UiO-66 was prepared by dispersing 2.0 mg of material in 2.0 mL of water under ultrasonication for 120 min. Subsequently, 5.0 µL of the suspension was drop-cast onto the cleaned GCE surface and dried at room temperature to obtain the Ho/UiO-66/GCE. For comparison, UiO-66/GCE and bare GCE were prepared using the same procedure.

Electrochemical measurements

Electrochemical experiments were carried out using a CPA-HH5 electrochemical analyser (Vietnam) equipped with a conventional three-electrode system consisting of a modified GCE as the working electrode, an Ag/AgCl (3 M KCl) electrode as the reference electrode, and a platinum wire as the counter electrode.

The electrochemical properties of the modified electrodes were evaluated by cyclic voltammetry (CV) in a solution containing 10 mM $[Fe(CN)_6]^{3-}/^{4-}$ and 0.1 M KCl.

The electrochemical determination of ACE and CIP was performed in 0.02 M Britton-Robinson buffer solution. Cyclic voltammetry was employed to investigate the electrochemical behaviour of the analytes, while differential pulse voltammetry (DPV) was used for quantitative analysis. The effects of pH, scan rate, accumulation potential, and accumulation time on the electrochemical response were systematically optimized.

Real sample analysis

The applicability of the present method was evaluated using real samples. Appropriate amounts of pharmaceutical samples were dissolved in deionized water and then diluted directly with Britton-Robinson buffer solution in the electrochemical cell before analysis. Quantitative determination was performed using the standard addition method. Recovery experiments were conducted by spiking known concentrations of ACE and CIP into the sample solutions to assess the accuracy of this procedure.

HPLC was employed as the reference method for the quantitative determination of ACE and CIP in pharmaceutical formulations. Chromatographic analyses were performed on a Shimadzu Series 30A HPLC system (Shimadzu, Japan) equipped with a diode array detector (DAD) and an InertSustain C18 column (150×4.6 mm, 5 µm). ACE was separated under isocratic conditions using a water/methanol/acetic acid mobile phase (69:28:3 volume ratio) at a flow rate of 0.6 mL min^{-1}, with ultraviolet (UV) detection at 275 nm. CIP was analysed using an isocratic mobile phase consisting of 0.025 M phosphoric acid (pH 3.0, adjusted

with triethylamine) and acetonitrile (85:15 volume ratio) at a flow rate of 0.5 mL min^{-1}, with detection at 278 nm. An injection volume of 20 µL was used for both analytes.

Results and discussion

Characterization of materials

Figure 1 presents the structural and textural characterization of UiO-66 and Ho/UiO-66 samples with different Ho/Zr molar ratios. As shown in Figure 1a, pristine UiO-66 exhibits the characteristic diffraction peaks of the UiO-66 framework, revealing the successful formation of the crystalline Zr-based MOF structure [28]. After Ho incorporation, the main diffraction features of UiO-66 are still retained, indicating that the parent framework is preserved. However, the diffraction peaks become progressively broader as the Ho content increases. The full width at half maximum (FWHM) increases from 0.265° for pristine UiO-66 to 0.696, 0.961, 1.435 and 2.730° for Ho/UiO-66 with Ho/Zr ratios of 1/100, 3/100, 5/100 and 7/100, respectively. Accordingly, the crystallite size calculated using the Scherrer equation [29] decreases markedly from 31.4 nm for UiO-66 to 11.9, 8.7, 5.8 and 3.0 nm for Ho/UiO-66 (1/100), Ho/UiO-66 (3/100), Ho/UiO-66 (5/100) and Ho/UiO-66 (7/100), respectively. This result reveals that incorporating Ho suppresses UiO-66 crystal growth and induces the formation of smaller crystallites with greater structural disorder. The absence of additional diffraction peaks related to crystalline Ho-containing phases indicates that Ho species are highly dispersed in the UiO-66 matrix or present in an amorphous/low-content form.

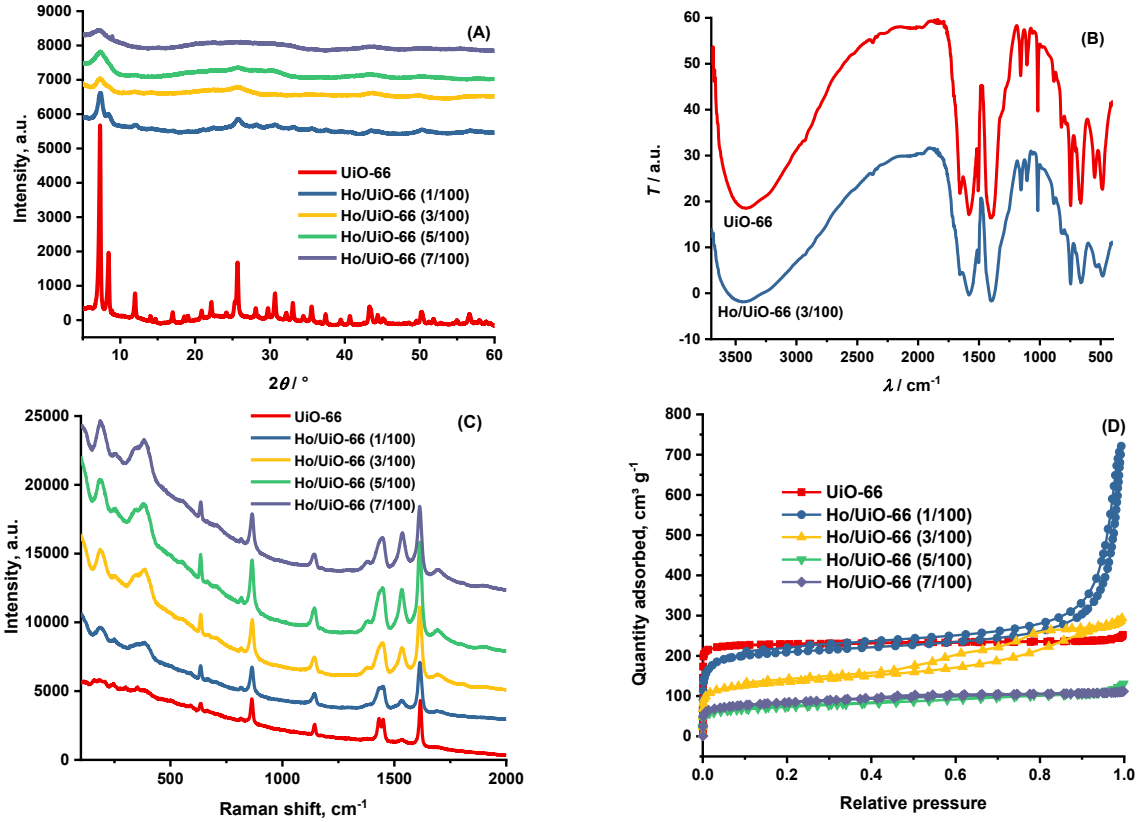

Figure 1. (A) XRD patterns, (B) FT-IR, (C) Raman spectra, (D) Nitrogen adsorption/desorption isotherms of UiO-66, Ho/UiO-66 (1/100), Ho/UiO-66 (3/100), Ho/UiO-66 (5/100) and Ho/UiO-66 (7/100)

The FT-IR spectra in Figure 1b further support the preservation of the UiO-66 framework after Ho incorporation. Pristine UiO-66 shows characteristic absorption bands at 3423, 2377, 1658, 1583, 1509, 1408, 1158, 1106, 1018, 883, 821, 751, 668, 554 and 484 cm^{-1} [30]. For Ho/UiO-66 (3/100), the corresponding bands are observed at 3440, 2377, 1658, 1579, 1500, 1395, 1155, 1102, 1018, 883, 821, 747, 664, 532 and 484 cm^{-1}. The bands at 1583/1579 and 1408/1395 cm^{-1} are assigned to the asymmetric and symmetric stretching

vibrations of coordinated carboxylate groups from terephthalate linkers [31]. The absence of a distinct C=O stretching vibration of free terephthalic acid near 1700 cm^{-1} indicates complete deprotonation and coordination of the organic linker to the metal clusters [32]. The bands at 751/747, 668/664, 554/532 and 484 cm^{-1} are associated with Zr-O and Zr-O-Zr vibrations of the $Zr_6O_4(OH)_4$ secondary building units [31,32]. The slight shifts from 1583 to 1579, 1408 to 1395, 751 to 747, 668 to 664 and 554 to 532 cm^{-1} after Ho incorporation reveal weak interactions between Ho species and the UiO-66 framework, while the overall similarity of the spectra verifies that the coordination structure of UiO-66 remains largely unchanged.

The Raman spectra shown in Figure 1c provide additional evidence for the structural integrity and local modification of UiO-66. Pristine UiO-66 exhibits Raman bands at 242, 297, 353, 633, 865, 1142, 1429, 1452, 1528 and 1619 cm^{-1}. After Ho incorporation, Ho/UiO-66 (3/100) displays bands at 184, 249, 342, 380, 633, 817, 862, 1144, 1379, 1447, 1533, 1611, 1691 and 1898 cm^{-1}. The bands at low wavenumbers are associated with vibrations of the inorganic Zr-O cluster, while the bands in the 1100-1650 cm^{-1} region arise mainly from vibrational modes of the terephthalate linker, including C-C, C=C, and carboxylate-related vibrations. The retention of the main Raman features, especially the bands at 633, 862-865, 1142-1144, 1447-1452, 1528-1533 and 1611-1619 cm^{-1}, reveals that the UiO-66 framework is preserved [30]. Meanwhile, the appearance of additional low-frequency bands at 184 and 249 cm^{-1} and the shifts of several linker-related bands, such as 1429 to 1379 cm^{-1} and 1619 to 1611 cm^{-1}, imply local structural distortion and possible Ho-O interactions induced by Ho incorporation. These results are consistent with the XRD observations of peak broadening and a reduction in crystallite size.

The N_2 adsorption-desorption isotherms in Figure 1d reveal significant changes in the textural properties of UiO-66 after Ho incorporation. Pristine UiO-66 possesses a high BET surface area of 685.7797 $m^2\ g^{-1}$, mainly contributed by micropores with a microporous surface area of 630.4662 $m^2\ g^{-1}$ and a mesoporous surface area of 55.3135 $m^2\ g^{-1}$. After Ho incorporation, the BET surface area decreases to 654.4211, 443.8458, 237.6775 and 274.2618 $m^2\ g^{-1}$ for Ho/UiO-66 (1/100), Ho/UiO-66 (3/100), Ho/UiO-66 (5/100) and Ho/UiO-66 (7/100), respectively. The microporous surface area also decreases markedly from 630.4662 $m^2\ g^{-1}$ for UiO-66 to 457.6689, 271.0899, 133.2476 and 155.1764 $m^2\ g^{-1}$ for the corresponding Ho/UiO-66 samples. In contrast, the mesoporous contribution increases after Ho incorporation, reaching 196.7522 $m^2\ g^{-1}$ for Ho/UiO-66 (1/100), compared with only 55.3135 $m^2\ g^{-1}$ for pristine UiO-66. These results indicate that Ho incorporation partially blocks the intrinsic micropores of UiO-66 and simultaneously generates additional interparticle mesoporosity due to the formation of smaller crystallites and structural defects. Overall, the combined XRD, FT-IR, Raman and BET results demonstrate that Ho species are successfully introduced into UiO-66 while the parent framework is largely preserved. The structural disorder, reduced crystallite size and modified pore structure induced by Ho incorporation may provide more accessible active sites and facilitate interfacial interactions in subsequent electrochemical applications.

The SEM image of pristine UiO-66 (Figure 2a) reveals the formation of uniformly distributed polyhedral nanoparticles with sizes in the nanometre range. The particles exhibit relatively regular morphology and tend to aggregate into larger clusters, which is typical for solvothermally synthesized UiO-66. The TEM image of Ho/UiO-66 (3/100) further confirms the nanoscale morphology and indicates that the particles remain well dispersed after Ho incorporation. No distinct Ho-rich particles are observed, demonstrating that Ho species are homogeneously distributed within the MOF matrix rather than forming separate phases. The EDX spectrum and elemental mapping results of Ho/UiO-66 (3/100) (Figure 2) clearly demonstrate the presence of C, O, Zr, and Ho elements. The uniform spatial distribution of these elements throughout the analysed region confirms the successful incorporation of Ho into the UiO-66 structure. The absence of localized Ho-rich domains further supports the conclusion that Ho species are highly dispersed within the framework, in agreement with the XRD and Raman results.

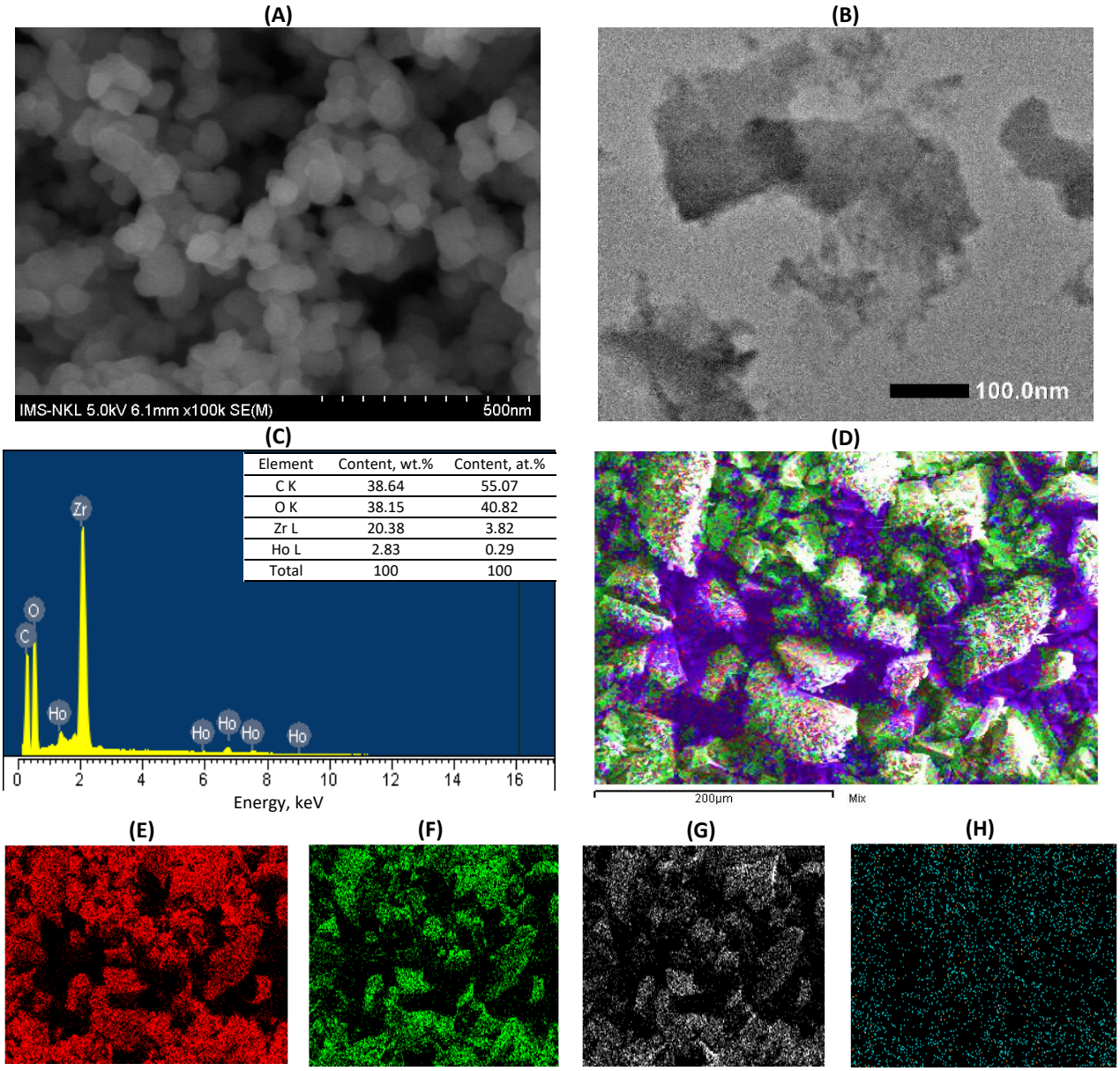

Figure 2. (A) SEM image of pristine UiO-66; (B) TEM image, (C) EDX spectrum and quantitative elemental composition, (D) merged EDX elemental mapping image, and individual elemental maps of (E) Zr, (F) O, (G) C and (H) Ho for Ho/UiO-66 (3/100)

Simultaneous electrochemical determination of acetaminophen and ciprofloxacin using holmium-modified UiO-66 metal-organic framework/glassy carbon electrode

Electrochemical behaviour of acetaminophen and ciprofloxacin at different electrodes

The electrochemical responses of ACE and CIP were investigated on bare GCE, UiO-66/GCE, and Ho/UiO-66-modified electrodes with different Ho contents. As shown in Figure 3, both ACE and CIP exhibited relatively weak oxidation signals at the bare GCE. Modification with UiO-66 resulted in a significant enhancement in peak currents, while further incorporation of Ho species led to an additional increase in the electrochemical response. Among all investigated electrodes, Ho/UiO-66 (3/100)/GCE exhibited the highest oxidation currents for both analytes and was therefore selected for subsequent experiments.

The high electrochemical performance of Ho/UiO-66 (3/100)/GCE can be attributed to the synergistic combination of the highly porous UiO-66 framework and the electroactive Ho species. The porous structure of UiO-66 facilitates analyte adsorption and mass transport, whereas Ho incorporation improves charge transfer and increases the density of active sites available for electron transfer.

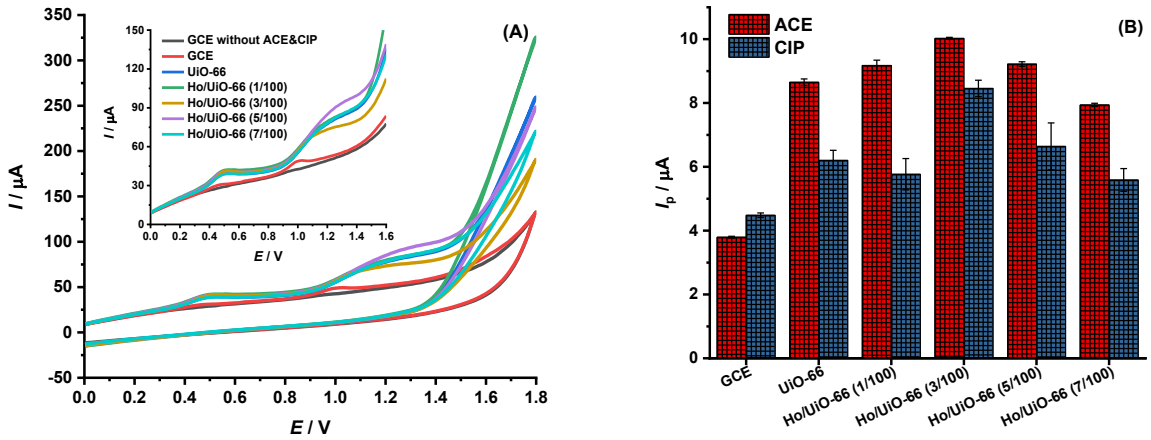

Figure 3. (A) CV curves of different electrodes recorded in 0.02 M BRS buffer (pH 6.0) containing 20 µM ACE and 20 µM CIP at a scan rate of 0.2 V s^{-1}; (B) Corresponding peak currents obtained at different electrodes from three repeated measurements

This interpretation is supported by the electrochemically active surface area (ECSA) measurements (Supplementary material, Figure S1). The ECSA values of bare GCE, UiO-66/GCE, and Ho/UiO-66 (3/100)/GCE were calculated to be 0.0362, 0.0465 and 0.0885 cm^2, respectively. The approximately 2.4-fold increase in ECSA compared with bare GCE indicates the formation of a substantially enlarged electroactive interface, which contributes directly to the enhanced oxidation currents observed for ACE and CIP.

Effect of pH

The influence of solution pH on the simultaneous determination of ACE and CIP was examined in BRS buffer over the pH range of 3-10 (Figure 4a).

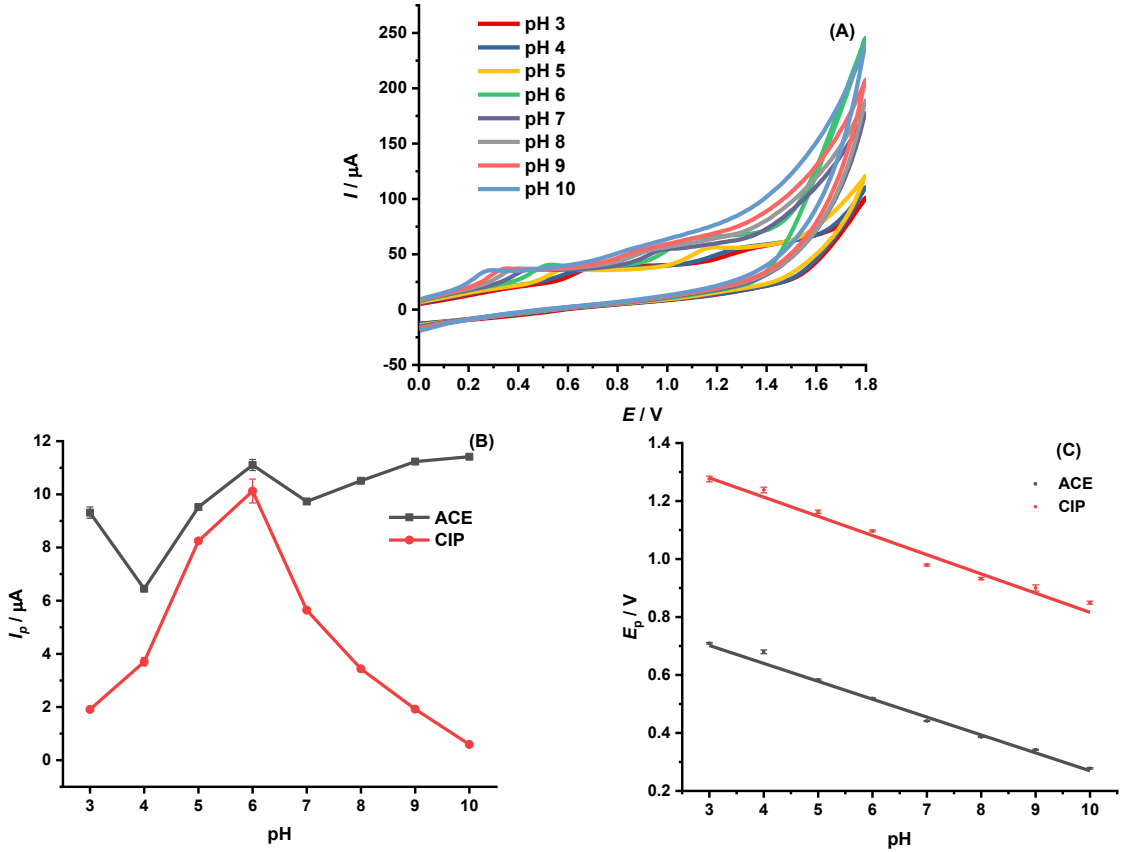

Figure 4. (A) CV curves of the Ho/UiO-66/GCE recorded in 0.02 M BRS buffer at different pH values (pH 3 to 10) containing 20 µM ACE and 20 µM CIP, at a scan rate of 0.2 V s^{-1}; (B) Variation of the peak currents with pH; (C) Dependence of the peak potentials on pH

The oxidation peak currents of both analytes strongly depended on pH, confirming the involvement of proton transfer during the electrochemical oxidation process. The oxidation current of ACE gradually increased with increasing pH, reaching a maximum near pH 5-6, whereas CIP exhibited a pronounced maximum at approximately pH 6. Beyond this pH value, the peak currents decreased, likely due to changes in the protonation state of the analytes and reduced adsorption efficiency on the electrode surface (Figure 4b). Therefore, pH 5 was selected as the optimum supporting electrolyte condition.

As shown in Figure 4c, the oxidation peak potentials shifted linearly toward less positive values with increasing pH, as described by Equations (1) and (2):

$E_{p,ACE}$ = 0.9086 - 0.0640pH (r^2 = 0.9913) (1)

$E_{p,CIP}$ = 1.4790 - 0.0653pH (r^2 = 0.9799) (2)

The slopes of approximately -64 mV pH^{-1} are close to the theoretical Nernstian value of -59 mV pH^{-1}, indicating that equal numbers of electrons and protons participate in the oxidation processes. This behaviour suggests that the electrochemical oxidation mechanisms of ACE and CIP involve proton-coupled electron transfer reactions.

Effect of scan rate and electrochemical oxidation mechanism

The effect of scan rate on the electrochemical behaviour of ACE and CIP was investigated by cyclic voltammetry over the range of 0.020 to 0.4 V s^{-1} (Figure 5a). As the scan rate increased, the oxidation peak currents increased proportionally, reflecting accelerated electron transfer and mass transport processes.

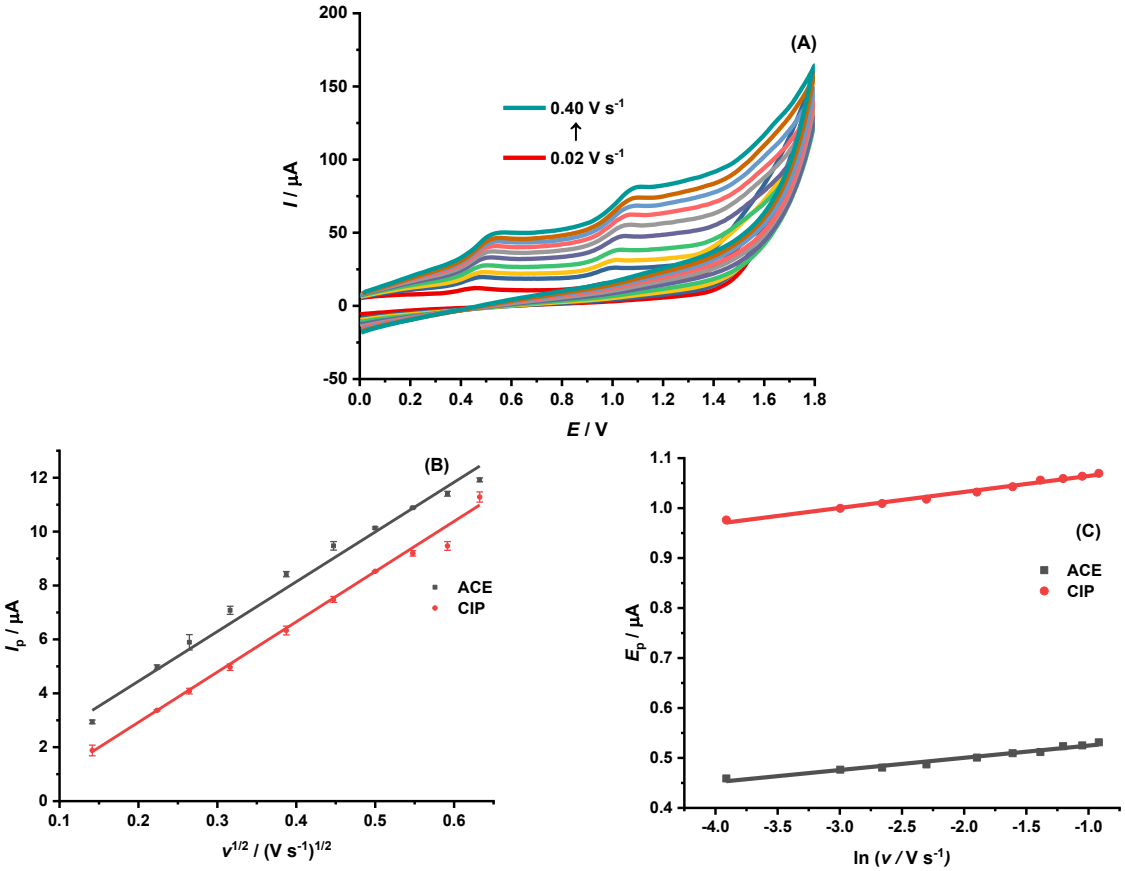

Figure 5. (A) CV curves of the Ho/UiO-66/GCE recorded in 0.02 M BRS buffer (pH 6.0) containing 20 µM ACE and 20 µM CIP at scan rates ranging from 20 to 400 mV s^{-1}; (B) Linear relationships between the peak currents and the square root of the scan rate ($v^{1/2}$); (C) Linear plots of the peak potentials of ACE and CIP versus ln *v*

As shown in Figure 5b, the oxidation peak currents exhibited linear relationships with the square root of the scan rate as follows in Equations (3) and (4):

$I_{p,ACE} = 1.0325 + 17.9647v^{1/2}$ ($r^2 = 0.9852$ (3)

$I_{p,CIP} = -0.7330 + 18.2407v^{1/2}$ ($r^2 = 0.9926$) (4)

These relationships indicate that the oxidation processes are predominantly diffusion-controlled [33]. The similar slopes obtained for ACE and CIP suggest comparable diffusion behaviour for both analytes at the Ho/UiO-66-modified surface. The oxidation peak potentials shifted toward more positive values with increasing scan rate, consistent with Laviron's equations, as expressed in Equations (5) and (6) [34]:

$E_{p,ACE} = 0.5492 + 0.0245\ln v$ ($r^2 = 0.9753$) (5)

$E_{p,CIP} = 1.09634 + 0.0320\ln v$ ($r^2 = 0.9888$) (6)

The calculated αn values were approximately 1.05 for ACE and 0.80 for CIP. Assuming a transfer coefficient $\alpha = 0.5$ for an irreversible system (Figure 5c) [33], the corresponding electron numbers were estimated to be approximately 2.1 and 1.6, respectively. Considering both the scan-rate analysis and the pH dependence study, the oxidation of ACE and CIP is reasonably assigned to a two-electron/two-proton process.

For ACE, the electrochemical oxidation occurs at the phenolic moiety and proceeds through the loss of two electrons and two protons to form N-acetyl-p-benzoquinone imine (NAPQI), as shown in Equation (7) [35,36]. This assignment is consistent with previous reports describing the ACE/NAPQI redox couple as a two-electron/two-proton process. Depending on the electrode surface and solution conditions, the electrogenerated NAPQI may be reduced back to ACE during the reverse scan; however, its subsequent chemical reactions can decrease the apparent reversibility of the overall process. The oxidation can be represented as:

$ACE \rightarrow NAPQI + 2H^+ + 2e^-$ (7)

For CIP, the anodic response is attributed to oxidation of the secondary amine nitrogen in the piperazine ring. According to the mechanism proposed in the cited literature, water participates in oxidative N-hydroxylation, producing an N-hydroxylated CIP derivative with the release of two electrons and two protons, as shown in Equation (8) [37,38]. The proposed reaction is:

$CIP + H_2O \rightarrow$ N-hydroxylated $CIP + 2H^+ + 2e^-$ (8)

Thus, the simultaneous anodic oxidation of ACE and CIP at the Ho/UiO-66/GCE is consistent with two distinct proton-coupled electron-transfer pathways. ACE is oxidized at the phenolic group to NAPQI, whereas CIP is proposed to undergo N-hydroxylation at the secondary nitrogen of the piperazine ring. In both cases, the near-Nernstian dependence of peak potential on pH, together with the scan-rate analysis, supports the participation of approximately equal numbers of electrons and protons, reasonably assigned as two electrons and two protons. The Ho/UiO-66-modified electrode provides accessible electroactive sites and promotes interfacial electron transfer, yielding two sufficiently separated oxidation peaks for simultaneous determination. Based on the present electrochemical results and the cited literature, the proposed oxidation pathways are illustrated in Scheme 1.

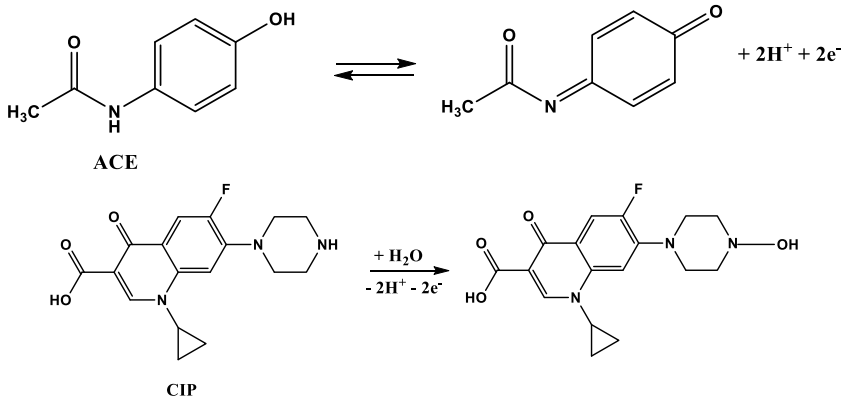

Scheme 1. Proposed electrochemical oxidation mechanisms of ACE and CIP at the Ho/UiO-66/GCE

Optimization of DPV parameters

To achieve maximum analytical sensitivity, the accumulation potential, accumulation time, pulse amplitude, and potential step were optimized. The highest combined peak currents for ACE and CIP were obtained at an accumulation potential of +0.2 V. More negative or positive potentials led to lower responses, indicating less favourable adsorption and preconcentration conditions. The influence of accumulation time revealed a rapid increase in current during the initial seconds, followed by a plateau. An accumulation time of 5 s was selected because longer accumulation periods provided negligible improvement while increasing analysis time.

The oxidation currents increased continuously with increasing pulse amplitude and reached their maximum values at 0.12 V. Similarly, the current response improved with increasing potential step and reached an optimum at 0.009 V. Consequently, the optimum DPV conditions were established as +0.2 V accumulation potential, 5 s accumulation time, 0.12 V pulse amplitude, and 0.009 V potential step (Figure S2 to S5).

Analytical performance

Under optimized conditions, well-defined and completely separated oxidation peaks corresponding to ACE and CIP were obtained. As shown in Figure 6, the peak currents increased systematically with analyte concentration over two linear concentration ranges as follows: Equations (9) and (10):

For the first concentration range (0.50 to 4.95 µM):

$I_{p,ACE} = 0.99454 + 0.61132C_{ACE}$ ($r^2 = 0.998$) (9)

$I_{p,CIP} = 0.40152 + 0.63803C_{CIP}$ ($r^2 = 0.9983$) (10)

At higher concentrations (4.95 to 23.81 µM), a second linear region was observed, as described by Equations (11) and (12):

$I_{p,ACE} = 2.5595 + 0.2742C_{ACE}$ ($r^2 = 0.9993$) (11)

$I_{p,CIP} = 2.4401 + 0.2387C_{CIP}$ ($r^2 = 0.9982$) (12)

The limits of detection (LOD) were calculated from the first linear range using Equation (13)

$LOD = 3\sigma/b$ (13)

where σ is the residual standard deviation of the linear regression based on the five lowest concentration points (inset of Figure 6b), and b is the slope of the corresponding calibration curve. The obtained LOD values were 0.14 µM for ACE and 0.13 µM for CIP.

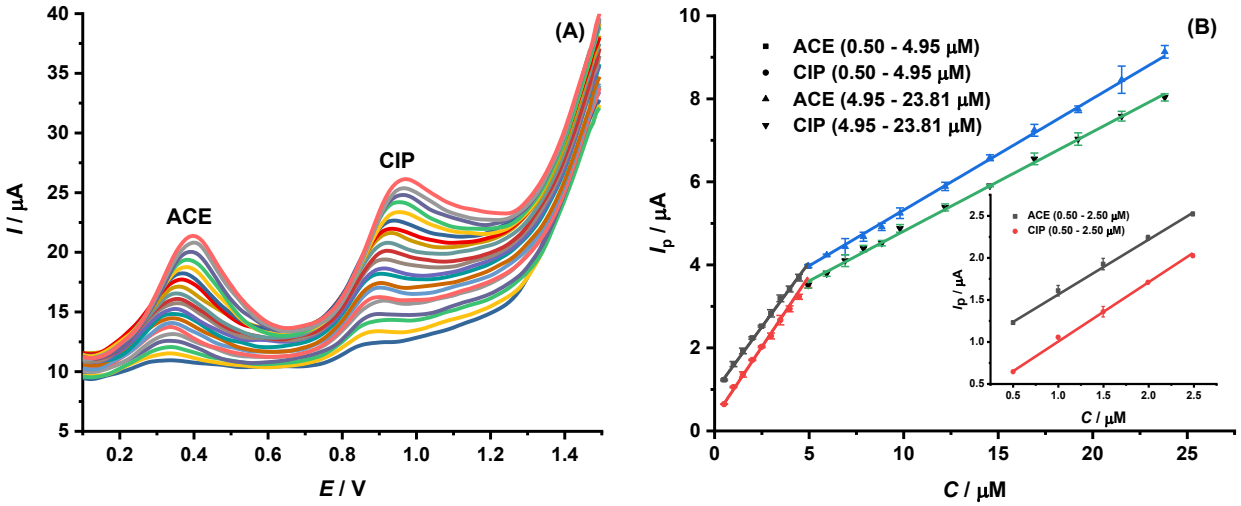

Figure 6. (A) DPV curves of the Ho/UiO-66/GCE recorded in 0.02 M BRS buffer (pH 5.0) containing ACE and CIP at concentrations ranging from 0.50 to 23.81 µM; (B) Calibration plots showing the linear relationships between the peak currents and the concentrations of ACE and CIP

The lower sensitivities observed in the second concentration range are likely associated with partial saturation of active adsorption sites and slower diffusion of analytes to the electrode surface at elevated concentrations. Nevertheless, high linearity was maintained throughout the investigated concentration range, demonstrating the suitability of Ho/UiO-66/GCE for quantitative analysis.

A comparison of the analytical performance of this Ho/UiO-66/GCE with previously reported electrochemical sensors is presented in Table 1. The developed sensor exhibited low detection limits of 0.14 μM for ACE and 0.13 μM for CIP, comparable to or lower than those reported for conventional GCE and several MOF-based electrodes. For example, the LOD obtained for ACE is lower than that of bare GCE (0.369 μM) and comparable to that reported for Zn-MOF/GCE (0.104 μM). For CIP determination, the analytical performance of Ho/UiO--66/GCE is similar to that of cobalt-based coordination polymer electrodes and TiO_2/PB/AuNPs/CMK-3/Nafion--modified electrodes. Although some advanced sensors, such as CZF/CME, exhibit lower detection limits, they generally involve more complicated fabrication procedures and require stripping voltammetric techniques. In contrast, the present Ho/UiO-66/GCE provides a simple preparation procedure, satisfactory sensitivity, good peak separation, and successful application to pharmaceutical formulations. These results indicate that Ho incorporation into the UiO-66 framework effectively improves the electrochemical response toward both ACE and CIP and offers a promising platform for the simultaneous determination of pharmaceutical compounds.

Table 1. Comparison of the analytical performance of the proposed Ho/UiO-66/GCE with previously reported electrochemical sensors for the determination of ACE and CIP

Electrode	Method	LOD, μM		Linear range, μM		Real samples	Ref.
		ACE	CIP	ACE	CIP		
GCE	DPV	0.369	-	4 to 100	-	Pharmaceutical formulations	[39]
Zn-MOF/GCE	DPV	0.104	-	1 to 50	-	Real blood samples	[40]
GPA-PVPy/GC	DPV	-	9.0	-	10 to 310	Urine samples	[38]
{[Co(HL)(bix)]·H_2O}n/GCE	DPV	-	0.135	-	2- to 20	Real water samples	[41]
{[Co(HL)(bimb)]·H_2O}n/GCE	DPV	-	0.082	-	1 to 14	Real water samples	[41]
TiO_2/PB/AuNPs/CMK-3/ /Nafion/GE	CV	0.108	0.210	1 to 10; 10 to 52	1 to 10; 10 to 52	Environmental water	[42]
CZF/CME	AdSDPV	0.0085	0.0026	0.185 to 476	0.0909 to 4700	Pharmaceutical formulations, serum and urine samples	[43]
C-HAP/GCE	SWV	0.1397	0.0918	0.01 to 1310	0.01 to 1310	Pharmaceutical drugs and biological samples	[44]
Ho/UiO-66/GCE	DPV	0.14	0.13	0.50 to 4.95; 4.95 to 23.81	0.50 to 4.95; 4.95 to 23.81	Pharmaceutical formulations	This work

Zn-MOF: Zn-based metal-organic framework; GPA-PVPy: Polyaniline-poly(vinylpyrrolidone)-graphene; {[Co(HL)(bix)]·H_2O}$_n$ and {[Co(HL)(bimb)]·H_2O}$_n$: two Co(II)-based coordination polymers; TiO_2/PB/AuNPs/CMK-3/Nafion: titanium dioxide sol enriched with mesoporous carbon CMK-3, gold nanoparticles and Nafion; CZF/CME: copper zinc ferrite nanoparticles modified carbon paste electrode; C-HAP: cuttlefish bone-derived hydroxyapatite sub-microparticles; AdSDPV: adsorptive stripping differential pulse voltammetry; SWV: Square wave voltammetry

Repeatability, reproducibility and stability

The analytical precision of the developed sensor was evaluated using five concentration levels ranging from 1.0 to 14.6 μM. The relative standard deviation (RSD) values for both analytes were below 5% and considerably lower than one-half of their corresponding Horwitz values, indicating high repeatability (Figure 7a).

The long-term stability of the modified electrode was evaluated over ten consecutive days (Figure 7b). The obtained RSD values were 1.38 % for ACE and 1.76 % for CIP, demonstrating high storage stability. Reproducibility, assessed using ten independently prepared electrodes, yielded RSD values of 2.17 % and 2.21 % for ACE and CIP, respectively (Figure 7c). These results demonstrate that the fabrication procedure is highly reproducible and that the Ho/UiO-66 coating remains stable during prolonged use.

Interference study

The selectivity of this sensor was evaluated in the presence of various potentially interfering species, including inorganic ions (Zn^{2+}, Ca^{2+}, Na^{+}, Al^{3+}, Fe^{3+}), carbohydrates (glucose, sucrose, lactose), amino acids

(glutamic acid), and common pharmaceutical additives (caffeine, sodium benzoate, citric acid) (Figure 7d). Even at concentrations 100-fold higher than those of ACE and CIP, most interfering compounds produced signal variations below ±10 %. Although Zn^{2+} and Al^{3+} caused slightly larger changes in the ACE signal, the overall recovery remained acceptable, and no significant overlap of oxidation peaks was observed. These findings demonstrate the high selectivity of the Ho/UiO-66/GCE sensor and verify its suitability for analysis of complex pharmaceutical matrices.

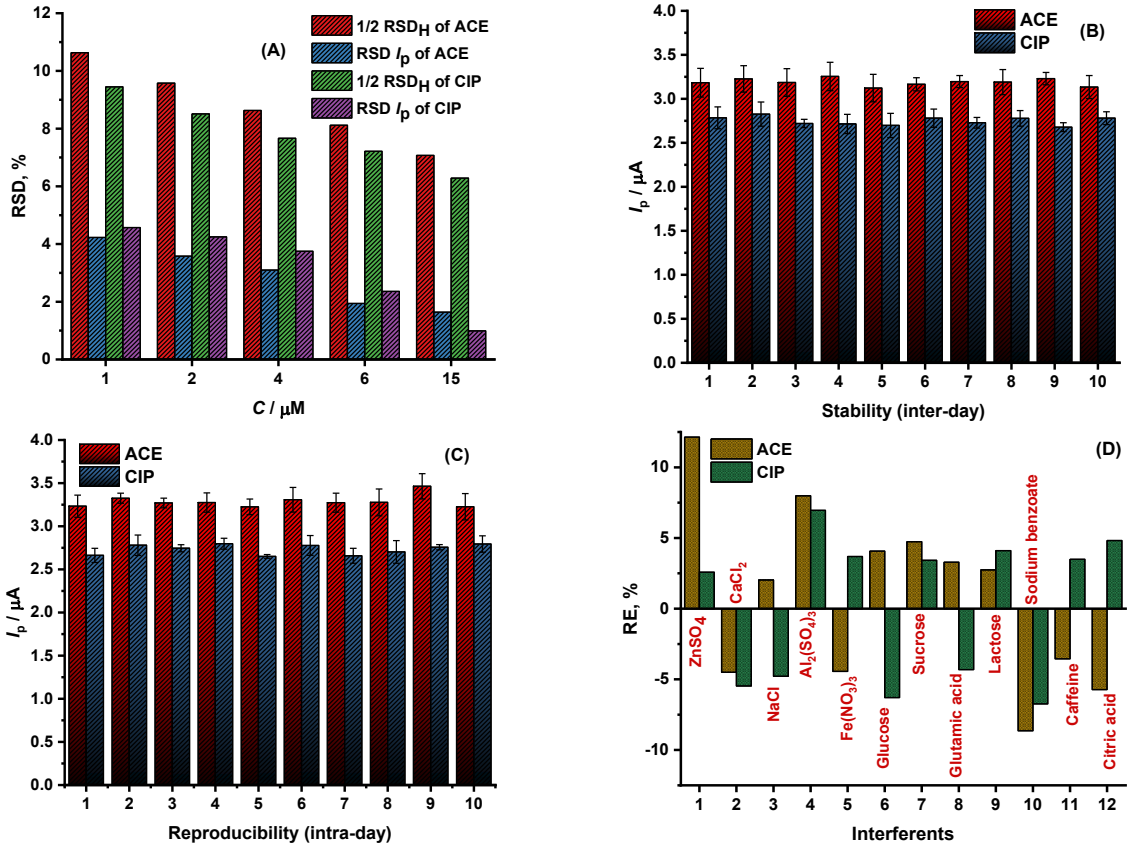

Figure 7. (A) Comparison of the RSD values of the peak currents for ACE and CIP at concentrations of 1.0, 2.0, 4.0, 5.9, and 14.6 μM with the corresponding ½ Horwitz RSD values; (B) Peak current responses for 4.0 μM ACE and CIP in 0.02 M BRS buffer (pH 6.0) at the Ho/UiO-66-modified electrode over a 10-day period, demonstrating long-term stability; (C) Peak current responses obtained from ten independently prepared Ho/UiO-66-modified electrodes, demonstrating fabrication reproducibility and (D) Relative errors (RE, %) obtained for the simultaneous determination of ACE and CIP in the presence of various potentially interfering substances

Analysis of pharmaceutical samples

The practical applicability of this Ho/UiO-66/GCE sensor was evaluated through the simultaneous determination of ACE and CIP in commercial pharmaceutical formulations. As shown in Table 2, the contents determined by the developed DPV method were in close agreement with those obtained by the reference HPLC method. For ACE-containing samples, the determined content ranged from 244.9 ± 2.1 to 636.3 ± 9.3 mg, while the corresponding HPLC values ranged from 240.3 to 643.5 mg. Similarly, for CIP-containing samples, the content obtained by DPV varied from 244.7 ± 2.8 to 506.9 ± 3.1 mg, which were very close to the values determined by HPLC from 249.5 to 499.5 mg. To further evaluate the accuracy of this method, the results obtained by DPV and HPLC were statistically compared using a paired samples t-test. The statistical analysis revealed no significant difference between the two methods at the 95 % confidence level, demonstrating the reliability and accuracy of the developed electrochemical method for the determination of ACE and CIP in pharmaceutical formulations. The accuracy of the developed sensor was further assessed by the standard addition method. Recovery values ranged from 94.3 to 103.6 % for ACE and from 96.6 to 104.5 % for CIP, supporting satisfactory accuracy and negligible matrix interference. Moreover, the low standard deviation

values obtained for all samples demonstrate acceptable precision and repeatability of this analytical procedure. These results reveal that the Ho/UiO-66/GCE sensor can be applied for the simultaneous determination of ACE and CIP in real pharmaceutical samples.

Table 2. Determination of ACE and CIP in pharmaceutical samples by the present DPV method and comparison with HPLC results. Recovery values were obtained by the standard addition method

Samples	Analyte	Content ± SD, mg		Concentration, µM		Recovery, %
		HPLC*	DPV**	Spiked	Found ± SD	
ACE Powder for oral (label claim: 250 mg ACE *per* unit)	ACE	240.3	244.9 ± 2.1	0.50	0.4777 ± 0.0086	95.5
ACE Tablet 1 (label claim: 500 mg ACE *per* unit)	ACE	505.0	510.1 ± 3.8	0.50	0.4714 ± 0.0055	94.3
ACE Tablet 2 (label claim: 650 mg ACE *per* unit)	ACE	643.5	636.3 ± 9.3	0.50	0.5145 ± 0.0159	103.6
CIP Powder for oral (label claim: 250 mg CIP *per* unit)	CIP	249.5	244.7 ± 2.8	0.50	0.5224 ± 0.0094	104.5
CIP Tablet 1 (label claim: 500 mg CIP *per* unit)	CIP	488.5	485.3 ± 5.8	0.50	0.4828 ± 0.0108	96.6
CIP Tablet 2 (label claim: 500 mg CIP *per* unit)	CIP	499.5	506.9 ± 3.1	0.50	0.5141 ± 0.0088	102.8

*Reference HPLC method; ** Proposed DPV method

Conclusion

A series of Ho-modified UiO-66 materials with different Ho/Zr molar ratios were successfully synthesized via a solvothermal method and systematically evaluated as electrode modifiers for the simultaneous electrochemical determination of ACE and CIP. Structural characterization demonstrated that Ho incorporation preserved the crystalline UiO-66 framework while inducing reduced crystallite size, increased structural defects, and modified pore characteristics. Among the investigated materials, Ho/UiO-66 (3/100) exhibited the optimum balance between structural integrity and electrochemical activity, resulting in the highest analytical response toward both analytes. The enhanced sensing performance can be attributed to the synergistic effects of Ho incorporation, which increased the electrochemically active surface area, introduced additional electroactive sites, and facilitated interfacial charge-transfer processes. Under the optimized DPV conditions, the developed Ho/UiO-66/GCE enabled well-separated oxidation peaks for ACE and CIP, providing two wide linear concentration ranges (0.50 to 4.95 and 4.95 to 23.81 µM) with low detection limits of 0.14 and 0.13 µM, respectively. The sensor also exhibited satisfactory selectivity, repeatability, reproducibility, long-term stability, and excellent analytical performance in pharmaceutical formulations, with results in good agreement with those obtained by the reference HPLC method. Overall, this study demonstrates that rare-earth modification is an effective strategy for tailoring the physicochemical and electrochemical properties of UiO-66. The proposed Ho/UiO-66/GCE provides a simple, reliable, and sensitive platform for the simultaneous determination of pharmaceutical compounds and offers valuable insights into the rational design of rare-earth-functionalized MOF-based electrochemical sensors for future analytical applications.

Supplementary material

Additional data are available at https://pub.iapchem.org/ojs/index.php/admet/article/view/3535, or from the corresponding author on request.

Contribution statement: *N. Q. Man, P. T. H. T and L. L. Son: data curation, methodology, investigation, formal analysis, funding acquisition, writing - original draft; P. T. Quy, T. T. P. Nga, L. V. T. Son and C. V. Hoang: Investigation, visualization, validation; D. Q. Khieu, P. K. Lieu and L. T. H. Phong: conceptualization, supervision, writing - review & editing. All authors read and approved the final manuscript.*

Conflict of interest: *The authors declare they have no conflict of interest.*

Funding*: The authors thank the Ministry of Education and Training, Vietnam, for their financial support under the Project No. B 2024-DHH-05, as well as Hue University under the core research program No. NCTB. DHH.2025.05*

Author statement: *The data will be made available upon request.*

References

[1] E.B. Gram, M. Bliddal, S. Pflugfelder, P.B. Jensen, P. Damkier. Prescription use of acetaminophen

among pregnant women in Denmark from 2000 to 2023: A drug utilization study. *British Journal of Clinical Pharmacology* **92** (2026) 556-567. https://doi.org/10.1002/bcp.70296

[2] E. Yoon, A. Babar, M. Choudhary, M. Kutner, N. Pyrsopoulos. Review Article Acetaminophen-Induced Hepatotoxicity : a Comprehensive Update. *Journal of Clinical and Translational Hepatology* **4** (2016) 131-142. http://dx.doi.org/10.14218/JCTH.2015.00052

[3] U.O. Kibwana, J. Manyahi, D.M. Sabas, R. Chande, G. Bwire, S.J. Moyo, S.E. Mshana. Ciprofloxacin resistance in community and hospital-acquired urinary tract infections: a systematic review and meta-analysis from African population. *BMC Infectious Diseases* **26** (2025) 212. http://dx.doi.org/10.1186/s12879-025-11546-6

[4] J. Chen. Real-world pharmacovigilance assessment of ciprofloxacin hydrochloride tablets using the FDA adverse event reporting system (January 1, 2014 to June 30, 2024). *Journal of Pharmaceutical Health Services Research* **17** (2026) rmag006. http://dx.doi.org/10.1093/jphsr/rmag006

[5] M.D. Harfiansyah, G.A.C. Purba, F. Fitria, U.K. Rambe, A.A. Amar. Validation of an HPLC Analytical Method for the Determination of Paracetamol in Generic and Branded Tablet Dosage Forms. *Journal of Pharmaceutical and Sciences* **8** (2025) 3032-3038. http://dx.doi.org/10.36490/journal-jps.com.v8i4.1107

[6] M.M. Eraqi, A.M. Algohary, Y.O. Al-Ghamdi, A.M. Ibrahim. Simultaneous spectrophotometric determination of paracetamol, tramadol, and aceclofenac in Pharmaceuticals: A green method with an adaptive plateau-based successive projections algorithm with automated tuning of support vector regression. *Sustainable Chemistry and Pharmacy* **46** (2025) 102056. https://doi.org/10.1016/j.scp.2025.102056

[7] P.R. Rajguru, R.D. Chakole, I.D. Gonjari, K.R. Mali, D.M. Chaudhari, K.S. Bansode. RP-HPLC Method Development for Simultaneous Estimation of Paracetamol and Nefopam in Spiked Human Plasma Using a Design of Experiments Approach. *Journal of Pharmaceutical Innovation* **21** (2026) 534. http://dx.doi.org/10.1007/s12247-026-10744-2

[8] A. More, B. Shetkar, K. Satpute, S.M. Syed. Development and validation of a green RP-HPLC method for simultaneous estimation of paracetamol and caffeine in tablets using quality by design approach and ICH guidelines. *Discover Applied Sciences* (2026). http://dx.doi.org/10.1007/s42452-026-08824-6

[9] A.A. Kulkarni, K. Mohanraj. Development and validation of an LC-MS/MS method for quantification of paracetamol and camylofin in human serum. *Future Journal of Pharmaceutical Sciences* **11** (2025) 128. http://dx.doi.org/10.1186/s43094-025-00886-4

[10] P. Kubalczyk, I. Kośka, R. Głowacki. HPLC and CE Procedures for the Determination of Fluoroquinolones (2020-2025). *Molecules* **31** (2026) 651. http://dx.doi.org/10.3390/molecules31040651

[11] M.F. Khan, M.A. Sheraz, S. Ahmed, Z. Anwar, S.F. Ahsan, A. Sabah, R. Ali, S.H. Kazi. Spectrofluorimetric and Spectrophotometric Methods for the Determination of Ciprofloxacin HCl and Their Comparison with the Compendial High-Performance Liquid Chromatography (HPLC) Method. *Anti-Infective Agents* **24** (2026) 30-50. http://dx.doi.org/10.2174/0122113525386386250704103943

[12] A. Shamim, M.J. Ansari, A. Aodah, M. Iqbal, M. Aqil, M.A. Mirza, Z. Iqbal, A. Ali. QbD-Engineered Development and Validation of a RP-HPLC Method for Simultaneous Estimation of Rutin and Ciprofloxacin HCl in Bilosomal Nanoformulation. *ACS Omega* **8** (2023) 21618-21627. http://dx.doi.org/10.1021/acsomega.3c00956

[13] K. Jagani, Y.R. Singh, E. Patel, R. Jani, S. Shah, P. Patel, D. Maheshwari, J. Shah, D. Shah. Coupling analytical method validation with machine learning for mobile phase prediction in RP-HPLC. *Discover Chemistry* **3** (2026) 371. http://dx.doi.org/10.1007/s44371-026-00828-w

[14] M.K. Matta, A. Chockalingam, A. Gandhi, S. Stewart, L. Xu, K. Shea, V. Patel, R. Rouse. LC-MS/MS based quantitation of ciprofloxacin and its application to antimicrobial resistance study in Balb/c mouse plasma, urine, bladder and kidneys. *Analytical Methods* **10** (2018) 1237-1246. http://dx.doi.org/10.1039/C7AY02923C

[15] I. Varenina, N. Bilandžić, J. Kaurinović, M. Đokić, M. Sedak, B. Solomun Kolanović, B. Čalopek, D. Vratarić, I. Varga. Validation of an LC-MS/MS multi-residue method for nine antibiotic classes in eggs according to EU regulation 2021/808 and assessment of their occurrence on Croatian poultry farms . *Food Additives & Contaminants: Part A* **43** (2026) 348-360. http://dx.doi.org/10.1080/19440049.2026.2623137

[16] F. Sadeghi-chahnasir, F. Amiripour, S. Ghasemi. Ratiometric fluorescence assay for ciprofloxacin in human blood serum and urine samples based on sulfur-doped carbon dots/rhodamine B nanohybrid encapsulated HKUST-1 metal-organic framework. *Talanta* **286** (2025) 127477. https://doi.org/10.1016/j.talanta.2024.127477

[17] H. El Kojok, N. El Darra, M. Khalil, A. Capo, A. Pennacchio, M. Staiano, A. Camarca, S. D'Auria, A. Varriale. Fluorescence polarization assay to detect the presence of traces of ciprofloxacin. *Scientific Reports* **10** (2020) 4550. http://dx.doi.org/10.1038/s41598-020-61395-3

[18] M.K. Muthukumaran, M. Govindaraj, S. Kogularasu, B. Sriram, B.K. Raja, S.-F. Wang, G.-P. Chang-Chien, A. Selvi J. Recent advances in metal-organic frameworks for electrochemical sensing applications. *Talanta Open* **11** (2025) 100396. https://doi.org/10.1016/j.talo.2024.100396

[19] M. Arivazhagan, S. Prabu, M. Elancheziyan, J. Jakmunee. Recent advances and future perspectives in electrochemical sensing of biomarkers by using MOF- based electrode materials. *Emergent Materials* **8** (2025) 1067-1085. http://dx.doi.org/10.1007/s42247-024-00941-5

[20] J. Winarta, B. Shan, S.M. Mcintyre, L. Ye, C. Wang, J. Liu, B. Mu. A Decade of UiO-66 Research: A Historic Review of Dynamic Structure, Synthesis Mechanisms, and Characterization Techniques of an Archetypal Metal-Organic Framework. *Crystal Growth & Design* **20** (2020) 1347-1362. http://dx.doi.org/10.1021/acs.cgd.9b00955

[21] D. Sheberla, J.C. Bachman, J.S. Elias, C.-J. Sun, Y. Shao-Horn, M. Dincă. Conductive MOF electrodes for stable supercapacitors with high areal capacitance. *Nature Materials* **16** (2017) 220-224. http://dx.doi.org/10.1038/nmat4766

[22] Z. Fang, B. Bueken, D.E. De Vos, R.A. Fischer. Defect-Engineered Metal-Organic Frameworks. *Angewandte Chemie International Edition* **54** (2015) 7234-7254. https://doi.org/10.1002/anie.201411540

[23] M.A. Bujran, F. Dar, A. Tahir, B. Want. Terbium-doped metal-organic frameworks: Dielectric and ferroelectric properties with enhanced electrochemical sensing for heavy metal ion detection. *Journal of Solid State Chemistry* **341** (2025) 125100. https://doi.org/10.1016/j.jssc.2024.125100

[24] J.P. Vizuet, M.L. Mortensen, A.L. Lewis, M.A. Wunch, H.R. Firouzi, G.T. McCandless, K.J.J. Balkus. Fluoro-Bridged Clusters in Rare-Earth Metal-Organic Frameworks. *Journal of the American Chemical Society* **143** (2021) 17995-18000. http://dx.doi.org/10.1021/jacs.1c10493

[25] X. Shi, B. Cao, J. Liu, J. Zhang, Y. Du. Rare-Earth-Based Metal-Organic Frameworks as Multifunctional Platforms for Catalytic Conversion. *Small* **17** (2021) 2005371. https://doi.org/10.1002/smll.202005371

[26] X. Sun, K. Yuan, Y. Zhang. Advances and prospects of rare earth metal-organic frameworks in catalytic applications. *Journal of Rare Earths* **38** (2020) 801-818. https://doi.org/10.1016/j.jre.2020.01.012

[27] M.J. Katz, Z.J. Brown, Y.J. Colón, P.W. Siu, K.A. Scheidt, R.Q. Snurr, J.T. Hupp, O.K. Farha. A facile synthesis of UiO-66, UiO-67 and their derivatives. *Chemical Communications* **49** (2013) 9449-9451. http://dx.doi.org/10.1039/C3CC46105J

[28] A.A. Ansari, A.M. Khan, M.A.S. Salem, A.S. Bhat. Synthesis and characterization of Ni@UiO-66 Metal-Organic Framework for fluorescence detection of heavy metal ions in the aqueous phase. *Materials Chemistry and Physics* **318** (2024) 129245. https://doi.org/10.1016/j.matchemphys.2024.129245

[29] A.L. Patterson. The Scherrer formula for X-Ray particle size determination. *Physical Review* **56** (1939) 978-982. https://doi.org/10.1103/PhysRev.56.978

[30] C. Atzori, G.C. Shearer, L. Maschio, B. Civalleri, F. Bonino, C. Lamberti, S. Svelle, K.P. Lillerud, S. Bordiga. Effect of Benzoic Acid as a Modulator in the Structure of UiO-66: An Experimental and Computational Study. *The Journal of Physical Chemistry C* **121** (2017) 9312-9324. https://doi.org/10.1021/acs.jpcc.7b00483

[31] X. Sun, D. Hu, L. Yang, N. Wang, Y.-G. Wang, X. Ouyang. Efficient adsorption of Levofloxacin from aqueous solution using calcium alginate/metal organic frameworks composite beads. *Journal of Sol-Gel Science and Technology* **91** (2019) 353-363. https://doi.org/10.1007/s10971-019-05001-7

[32] L. Valenzano, B. Civalleri, S. Chavan, S. Bordiga, M.H. Nilsen, S. Jakobsen, K.P. Lillerud, C. Lamberti. Disclosing the Complex Structure of UiO-66 Metal Organic Framework: A Synergic Combination of

Experiment and Theory. *Chemistry of Materials* **23** (2011) 1700-1718. https://doi.org/10.1021/cm1022882

[33] A.J. Bard, L.R. Faulkner. Fundamentals and applications: electrochemical methods, 2nd ed., John Wiley & Sons, Ltd, New York, 2001.

[34] E. Laviron. General expression of the linear potential sweep voltammogram in the case of diffusionless electrochemical systems. *Journal of Electroanalytical Chemistry* **101** (1979) 19-28. https://doi.org/10.1016/S0022-0728(79)80075-3

[35] S. Mondal, M. Kumari, R. Madhuri, P.K. Sharma. Acetaminophen and acetone sensing capabilities of nickel ferrite nanostructures. *Applied Physics A* **123** (2017) 494. https://doi.org/10.1007/s00339-017-1107-y

[36] A.S. Farag. Voltammetric determination of acetaminophen in pharmaceutical preparations and human urine using glassy carbon paste electrode modified with reduced graphene oxide. *Analytical Sciences* **38** (2022) 1213-1220. https://doi.org/10.1007/s44211-022-00150-2

[37] S. Tajik, H. Beitollahi, R. Zaeimbashi, M. Sheikhshoaei, M.B. Askari, P. Salarizadeh. An electrochemical sensor based on V2O5 nanoparticles for the detection of ciprofloxacin. *Journal of Materials Science: Materials in Electronics* **32** (2021) 17558-17567. https://doi.org/10.1007/s10854-021-06288-5

[38] S. Perumal, R. Atchudan, K. Krukiewicz, A. Banaś, D.R. Kumar, H. Lee, W. Lee. Nanoarchitectonics of polyaniline-poly(vinyl pyrrolidone)-graphene composite for the electrochemical sensing of ciprofloxacin and uric acid. *Journal of the Taiwan Institute of Chemical Engineers* **172** (2025) 106103. https://doi.org/10.1016/j.jtice.2025.106103

[39] C. Engin, S. Yilmaz, G. Saglikoglu, S. Yagmur, M. Sadikoglu. Electroanalytical Investigation of Paracetamol on Glassy Carbon Electrode by Voltammetry. *International Journal of Electrochemical Science* **10** (2015) 1916-1925. https://doi.org/10.1016/S1452-3981(23)05122-2

[40] K.M. Ismail, S.S. Hassan, S.S. Medany, M.A. Hefnawy. A facile sonochemical synthesis of the Zn-based metal-organic framework for electrochemical sensing of paracetamol. *Materials Advances* **5** (2024) 5870-5884. https://doi.org/10.1039/D4MA00061G

[41] R. Xiang, T. Qin, Y. Liu, L. Lan, X. Dong, D. Srivastava, M.K. Parvez, M.S. Al-Dosari, A. Kumar, Y. Pan. Two novel cobalt-based coordination polymers for electrochemical sensing of trace ciprofloxacin. *Microchemical Journal* **209** (2025) 112594. https://doi.org/10.1016/j.microc.2024.112594

[42] A. Pollap, K. Baran, N. Kuszewska, J. Kochana. Electrochemical sensing of ciprofloxacin and paracetamol in environmental water using titanium sol based sensor. *Journal of Electroanalytical Chemistry* **878** (2020) 114574. https://doi.org/10.1016/j.jelechem.2020.114574

[43] M.P. Kingsley, P.K. Kalambate, A.K. Srivastava. Simultaneous determination of ciprofloxacin and paracetamol by adsorptive stripping voltammetry using copper zinc ferrite nanoparticles modified carbon paste electrode. *RSC Advances* **6** (2016) 15101-15111. https://doi.org/10.1039/C5RA19861E

[44] S. Anitta, C. Sekar. Voltammetric determination of paracetamol and ciprofloxacin in the presence of vitamin C using cuttlefish bone-derived hydroxyapatite sub-microparticles as electrode material. *Results in Chemistry* **5** (2023) 100816. https://doi.org/10.1016/j.rechem.2023.100816